



OPEN Tunable electronic and photoelectric properties of Janus group-III chalcogenide monolayers and based heterostructures

Yipeng Zhao¹, Qialai Tan²✉, Honglai Li³, Zhiqiang Li¹, Yicheng Wang¹ & Liang Ma¹✉

Janus group-III chalcogenide monolayers and based heterostructures with breaking vertical structural symmetry offer additional prospects in the upcoming high-performance photoelectric devices. We studied the geometrical, electronic, and photoelectric properties of Janus group-III chalcogenide monolayers and heterostructures. The most energy favorable stacking design of ten vertical heterostructures are considered. The results showed that the Janus Se-In-Ga-S and S-In-Ga-Se monolayers exhibit semiconducting characteristics with the band gaps of 1.295 eV and 1.752 eV, respectively. Furthermore, the different stacking configurations and surface termination at interface can realize the transition of band alignment between type I and type II due to the interlayer coupling. Moreover, we systematically investigated the photoelectric properties of Janus group-III chalcogenide heterostructures and predicated an optimized power conversion efficiency of 16.2%. These findings can aid in comprehending the customized characteristics of Janus group-III chalcogenide heterostructures, offering theoretical guidance for creating innovative photoelectric devices.

Since the successful exfoliation of graphene, two-dimensional (2D) materials have received worldwide interest due to their astonishingly physical properties and potential implementation in next-generation electronic and photoelectric devices^{1–5}. Among various 2D materials, group-III monochalcogenides (MX, M=Ga, In; X=S, Se) have received more attention in recent years due to their remarkable mechanical, electronic, and optical properties^{6–8}. The MX monolayers has a honeycomb lattice structure and stacking in the order of X-M-M-X. To date, various MX monolayers had been successfully synthesized, and it exhibited high carrier mobility, good metal contacts, high thermal stability, and the absence of dangling bond^{9–11}. All these merits make MX monolayers promising for photoelectric devices and improve the motivation to design heterostructures based on these materials^{12–14}. However, MX monolayers display relatively large indirect band gaps with 2.0–4.0 eV, resulting a poor absorption in the visible light spectrum^{15,16}. Thus, it is very important to find suitable means to realize effective tunable of electronic structure and optical properties in MX monolayer for its practical application^{17–21}.

Generally, the atom structure symmetry plays a crucial role in the determination of electronic properties for ultrathin materials^{22–25}. Due to its lattice asymmetry, the Janus monolayers has an intrinsic built-in electric field in the vertical direction compare with traditional MXs, which can separate the charge carriers and enhance the electron-phonon interaction^{26–28}. In addition, Janus MX monolayers showed distinct physical properties such as excellent absorption coefficient, high charge carrier mobility, and rapid separation of photogenerated carriers, which gives them potential for photovoltaic and photoelectric applications^{29,30}. For instance, the Janus In₂SSe monolayer possesses an indirect-direct bandgap transition due to the broken vertical symmetry³¹. Bui et al. systematically studied the structural, electronic, and optical properties of Janus Ga₂XY and In₂XY (Y = S, Se, Te) monolayers, and compared the acquired electronic band gaps with their binary analogs³². Zhong et al. have been predicted the dynamic stability of Janus Ga₂XY monolayer, and the phonon dispersions confirmed that the monolayers can exist as a freestanding structure³³. Furthermore, Ahmad et al. found that the band gaps

¹College of Physics and Electronic Engineering, Hengyang Normal University, Hengyang 421008, China. ²School of Physics and Electronic Electrical Engineering, Xiangnan University, Chenzhou 423000, China. ³College of Physics Science and Technology, Hebei University, Baoding 071002, People's Republic of China. ✉email: 492139003@qq.com; ml_hw@hotmail.com

of XGaInY monolayer extend from 0.74 to 2.66 eV, and the light absorption coefficients were greater than 10^4 cm^{-1} in the visible and ultraviolet region³⁴.

In addition, van der Waals (vdW) heterojunctions opens the way for new promising applications as they maintain the advantages of each monolayer and introduce new exciting properties due to the interlayer coupling^{35–37}. Inspired by the traditional 2D vdW heterojunctions, several attempts have been proposed to various heterostructures based on Janus monolayers to explore their novel properties^{38–40}. To date, numerous MX-based vdW heterostructures have been studied, such as $\text{In}_2\text{SeTe}/\text{Ga}_2\text{STe}$ and $\text{SeGa}_2\text{Te}/\text{SeIn}_2\text{Se}$ ^{41,42}. More interestingly, the MX-based vdWs heterostructures show the power conversion efficiency (PCE) up to 13.17%, while it further boosted to 21% in Janus $\text{In}_2\text{SeTe}/\text{Ga}_2\text{STe}$ lateral heterostructures⁴². In addition, the Janus- $\text{In}_2\text{SeTe}/\text{InSe}$ lateral heterostructures exhibit a high optical absorption coefficient of $8 \times 10^5 \text{ cm}^{-1}$ in visible light zone⁴³. Particularly, the combination of Janus monolayers gives birth to versatile heterostructures with magnificent properties such as excellent optical, tunable electrical contact properties, and etc^{44–46}.

Herein, we put forward first-principles simulations to examine the structure, electronic, photoelectric properties of Janus MX monolayers and MX-based heterostructures. Herein, we first evaluated the structural parameters and cohesive energy of Janus MX monolayers, and further investigated their electronic band structure and optical properties. Next, we construct ten vertical heterostructures of Janus MX with different stacking configurations, and investigated the electronic band structure and band diagrams of the most stable configurations. In addition, the enhanced light absorption of heterostructures is presented and the PCE of the heterostructures was evaluated. Our results establish that Janus MX and based heterostructures would be the probable candidates for electronic and photoelectric applications.

Computational details

All the first-principles computations within the framework of density-functional theory (DFT) were carried out by DS-PAW software. The Device Studio program provides several functions for performing visualization and modeling. We chose the generalized gradient approximation (GGA) in the Perdew–Burke–Ernzerhof (PBE) formalism to describe the exchange–correlation potential^{47–49}. A vacuum thickness of 20 Å (for single layer material) and 40 Å (for heterojunction) are built to avoid the interactions between adjacent layers. The Monkhorst–Pack k-point meshes of $9 \times 9 \times 1$ is used for geometric optimization and electronic structure calculation of Janus monolayers and heterojunction. A plane wave basis set with a cutoff energy of 500 eV was employed for plane wave expansion. In our calculations, the force and energy parameters of atomic relaxation are set as 0.01 eV/Å and 10^{-8} eV. To confirm the origin of the catalytic activity of vertical heterojunction, density of states (DOS) calculations and Bader charge analysis were performed. In the process of heterojunction optimization and computation, the DFT-D3 method with Grimme correction is adopted to describe the long-range van der Waals interactions⁵⁰. Additionally, the more accurate Heyd–Scuseria–Ernzerhof (HSE06) hybrid functional was employed to check the reliability of the band structure⁵¹.

Results and discussion

Figure 1a,b depicts the top and side view of atomic crystal structure in Janus Se-In-Ga-S and S-In-Ga-Se monolayers. Clearly, the Janus MX monolayer is made up of X-M-M'-X' configuration with broken mirror symmetry in the vertical direction. The optimized lattice constant, bond lengths and thicknesses after relaxation are listed in Table 1. The Ga-In bond lengths in the different Janus monolayers remain particularly unchanged, being similar to Ga–Ga and In–In bond lengths in traditional MX monolayer. In addition, the Bader charge analysis shows that the charge is transferred from metal atoms to chalcogenide atoms, as shown in Fig. 1c,d. For instance, the Ga and In atoms lose 0.773e and 0.706e for the Janus Se-In-Ga-S monolayer, while the Se and S atoms receive 0.662e and 0.818e, respectively. Actually, the Bader charge transfer is associated with the type of element and the bond length between the metal and chalcogenide atoms⁵². The bond length of M-S (M-Se) is 2.42 Å (2.62) in Janus Se-In-Ga-S and 2.52 Å (2.50) in S-In-Ga-Se monolayers, respectively. As can be seen in Fig. 1e,f, the calculated phonon spectra of Janus Se-In-Ga-S and S-In-Ga-Se monolayers shows no imaginary frequency, indicating its dynamic stability. The chalcogenide atoms attract electrons from metal atoms since the chalcogenide atoms are more electronegative⁵³. The different arrangements of metal and chalcogen atoms have noticeable effects on the charge transfer and electronic properties.

The electronic band structures of Janus Se-In-Ga-S and S-In-Ga-Se monolayers were calculated at the PBE and HSE06 level along the high symmetry points of M–K–Γ–K–M, as shown in Fig. 2a and b. Clearly, the Janus Se-In-Ga-S and S-In-Ga-Se monolayers preserve the semiconducting character, with the band gaps of 1.295 eV (2.14 eV) and 1.752 eV (2.61 eV) with the PBE (HSE06) functional, respectively. The PBE bandgap is always lower than the HSE06 bandgap. The band structure calculated using HSE06 hybrid functional are consistent with the results calculated using PBE functional for the type of band gap³⁴. The results show that the Se-In-Ga-S monolayers exhibit direct gaps with their valence band maximum (VBM) and conduction band minimum (CBM) points located at the Γ-point, while the S-In-Ga-Se monolayers are indirect band gap. Actually, the CBM of Se-In-Ga-S monolayers is main contributed by the *s* and *p_z* orbitals of Ga atoms and small contribution from *s* and *p_z*-orbitals of In atoms, and the VBM is mainly determined by the *p_x* and *p_y* orbitals of Se atoms. The CBM of S-In-Ga-Se monolayers is organized by the *s* orbitals of Ga atoms and small contribution from *s* orbitals of In and Se atoms, and the VBM is mainly determined by the *p_z* orbitals of S and Se atoms and small contribution from *p_z* orbitals of In and Ga atoms. The orbital-resolved band structures of Janus Se-In-Ga-S and S-In-Ga-Se monolayers show in Fig. S1. The band gap of MX can be effectively tuned by constructing the Janus structure, which provides an effective method to tailor the photoelectric properties of MX monolayers. In addition, Fig. 2c,d depicts the optical absorption coefficients of the Janus Se-In-Ga-S and S-In-Ga-Se monolayers as a function of photon energy. Obviously, the monolayers show considerable visible light and near-ultraviolet absorption, which can be ascribed

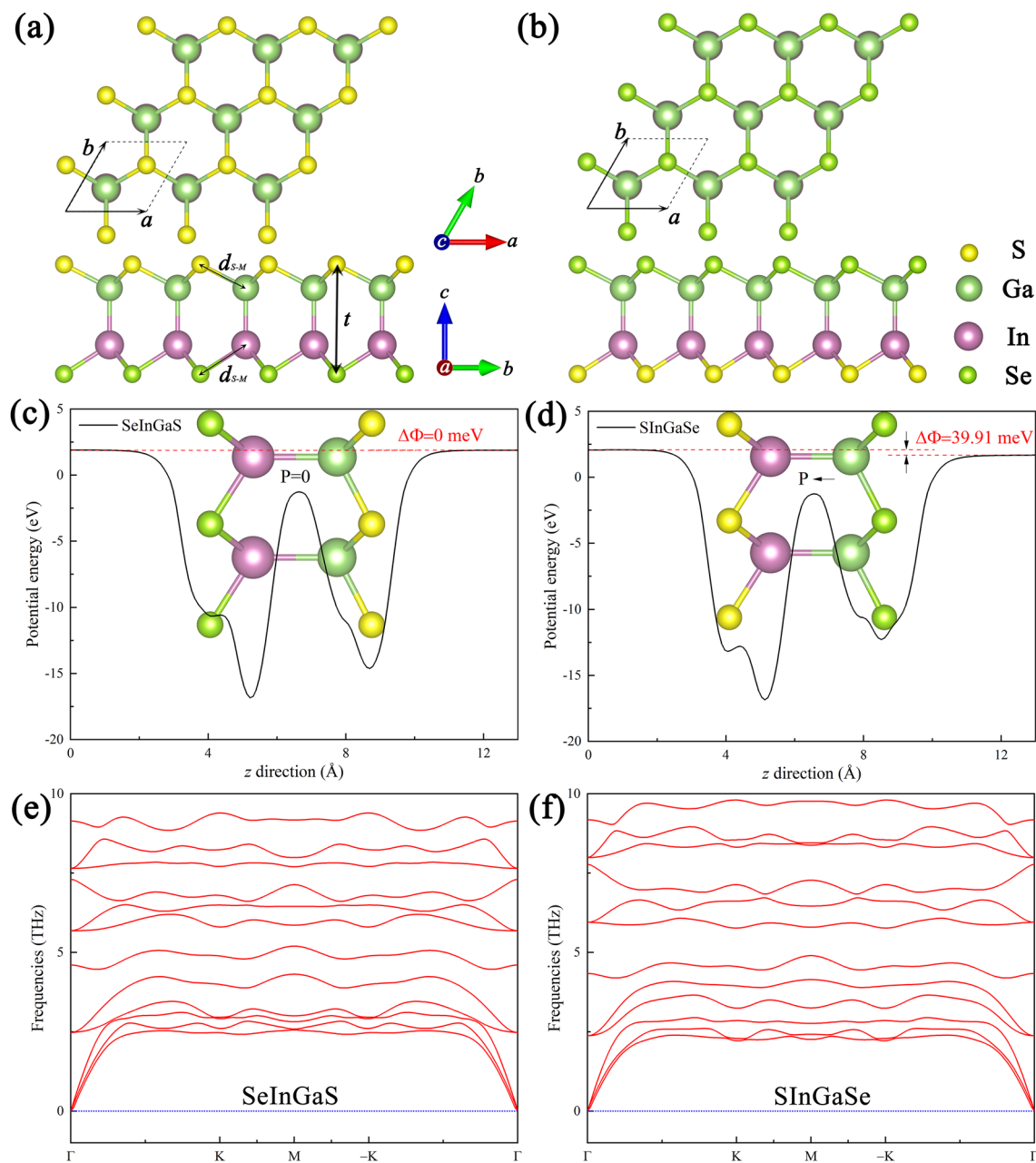


Figure 1. (a,b) Top view and side view of the Janus Se-In-Ga-S and S-In-Ga-Se monolayers. The average potential energy of the Janus Se-In-Ga-S (c) and S-In-Ga-Se (d) monolayers. The phonon spectrum of Janus Se-In-Ga-S (e) and S-In-Ga-Se (f) monolayers.

| Monolayer Janus | a (Å) | b (Å) | d_{S-M} (Å) | d_{Se-M} (Å) | t (Å) | E_g^{PBE} (eV) | E_g^{HSE06} (eV) |
|-----------------|---------|---------|---------------|----------------|---------|------------------|--------------------|
| Se-In-Ga-S | 3.82 | 3.82 | 2.42 | 2.62 | 5.03 | 1.29 | 2.14 |
| S-In-Ga-Se | 3.84 | 3.84 | 2.52 | 2.50 | 5.00 | 1.74 | 2.61 |

Table 1. Calculated lattice constant (a and b), layer spacing (d), S-M and Se-M chemical band length (d_{S-M} , d_{Se-M}), total thickness (t) and electronic band gap (E_g) using different exchange correlation functionals for monolayer Janus Se-In-Ga-S and S-In-Ga-Se.

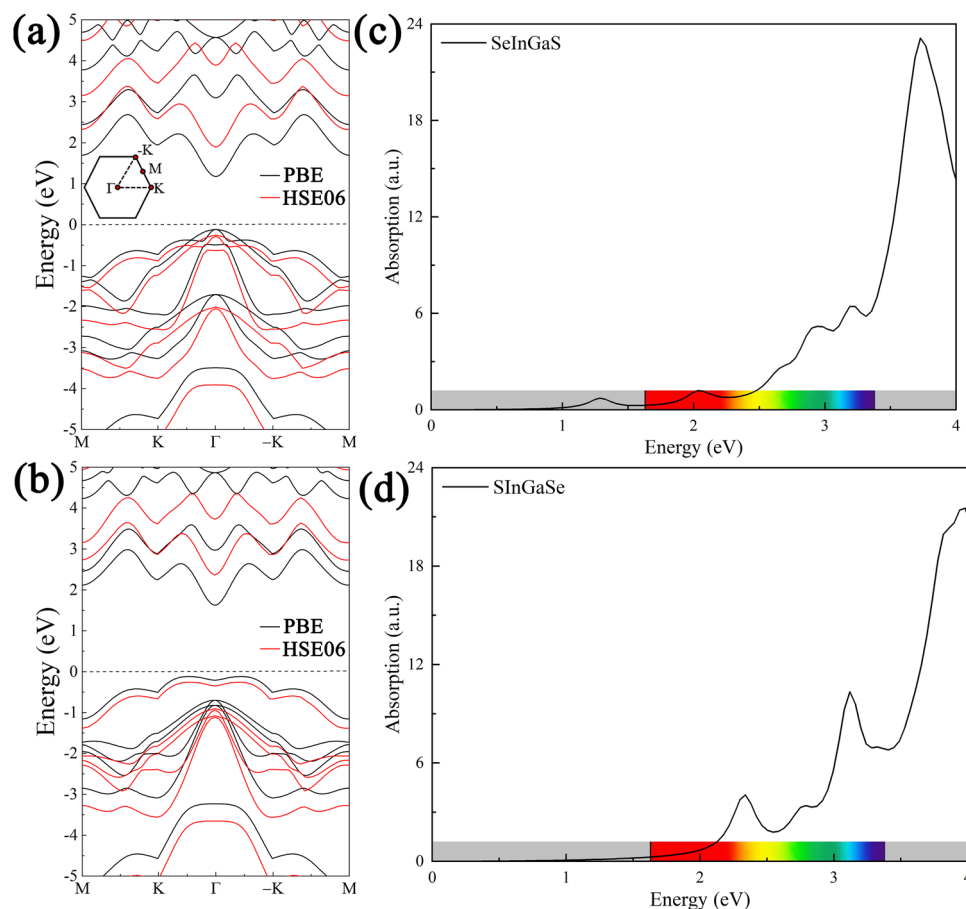


Figure 2. (a,b) The band structure calculated using PBE and HSE06 methods for the Janus Se-In-Ga-S and S-In-Ga-Se monolayers. The calculated optical absorption coefficients of the Janus Se-In-Ga-S (c) and S-In-Ga-Se (d) monolayers.

to the enhanced hybridization states near the VBM and the CBM. The excellent absorption coefficients in the visible region indicates that the Janus Se-In-Ga-S and S-In-Ga-Se monolayers are suitable for further applications.

The structure and stability properties of the heterostructures based on Se-In-Ga-S and S-In-Ga-Se were investigated. Since both the Janus Se-In-Ga-S and S-In-Ga-Se monolayers are mirror symmetry broken with two different terminated surfaces, here we construct totally 10 vertical configurations of heterostructure. Such as SSA, SSB, and SSC configurations, their commonality lies in the interlayer S element attached to each other (defined as SS), while their difference lies in the arrangement of metal element In and Ga. The atomic arrangement order and structural abbreviation of vertical heterojunctions are shown in Table 2. Furthermore, to check the energy stability of heterostructures, we calculated the binding energy: $E_{coh} = E_{SGaInSe/SeGaInS} - E_{SGaInSe} - E_{SeGaInS}$, where $E_{SGaInSe/SeGaInS}$ is the total energy of the heterostructure, $E_{SGaInSe}$ and $E_{SeGaInS}$ are the total energy of the isolated Se-In-Ga-S and S-In-Ga-Se monolayer, respectively. For SSA configurations, there have five different stacking patterns, shown in Fig 3. For all the configurations, the binding energies are all negative, and the most energy favorable stacking pattern are also listed in Table S1. The AB stacking has the smallest binding energies, which is most favorable stacking pattern. The calculated lattice parameter, equilibrium interlayer distance of favorable stacking pattern are also summarized in Table 3.

The electronic band structures of the vertical heterostructure with different stacking patterns are shown in Fig. 4a,d and Figs. S2, S3. The phonon spectra curves of SSA and SeSeB configuration are described in Fig. S4, and shows no imaginary frequency, which further verify the dynamical stabilities of these configuration. The heterostructures are indirect band gap semiconductors with the CBM located at Γ point and the VBM located near the Γ point of the Brillouin zone. The band gap of heterostructure with SSA configuration is 1.103 eV, which is smaller to the pristine Janus Se-In-Ga-S and S-In-Ga-Se monolayers. Clearly, the CBM of the heterostructures for SSA configuration is mainly contributed by the electronic states from the top layer, while the VBM is dominated by the bottom layer. Therefore, the type II band alignment of heterostructures can be found and the conduction band offset (CBO) between acceptor and donor is 0.176 eV, as shown in Fig. 4b,c. While for SeSeB configuration, the CBM is contributed by the top Se-In-Ga-S layer, and the VBM is dominated by the bottom S-In-Ga-Se layer, as shown in Fig. 4d,e. The band gap and CBO of SeSeB configuration are 1.039 eV and 0.271 eV, respectively. Typically, the type-II band alignment at interface allows the electrons and holes to be separated

| | Element order | Type | | | | | | | | | |
|--------------|---------------|------|-----|-----|-------|-------|-------|------|------|------|-------|
| | | SSA | SSB | SSC | SeSeA | SeSeB | SeSeC | SSeB | SSeA | SSeC | SSeB' |
| First layer | 1 | Se | Se | Se | S | S | S | Se | Se | Se | Se |
| | 2 | In | In | Ga | In | In | Ga | In | In | Ga | Ga |
| | 3 | Ga | Ga | In | Ga | Ga | In | Ga | Ga | In | In |
| | 4 | S | S | S | Se | Se | Se | S | S | S | S |
| Second layer | 5 | S | S | S | Se | Se | Se | Se | Se | Se | Se |
| | 6 | Ga | In | In | Ga | In | In | In | Ga | In | Ga |
| | 7 | In | Ga | Ga | In | Ga | Ga | Ga | In | Ga | In |
| | 8 | Se | Se | Se | S | S | S | S | S | S | S |

Table 2. SS: Interlayer S element is attached to S element; SeSe: Interlayer Se element is attached to Se element; A type: Two layers of material Ga element adhered to Ga element; B type: Two layers of material Ga element adhered to In element; B' type: Two layers of material In element adhered to Ga element; C type: Two layers of material In element adhered to In element.

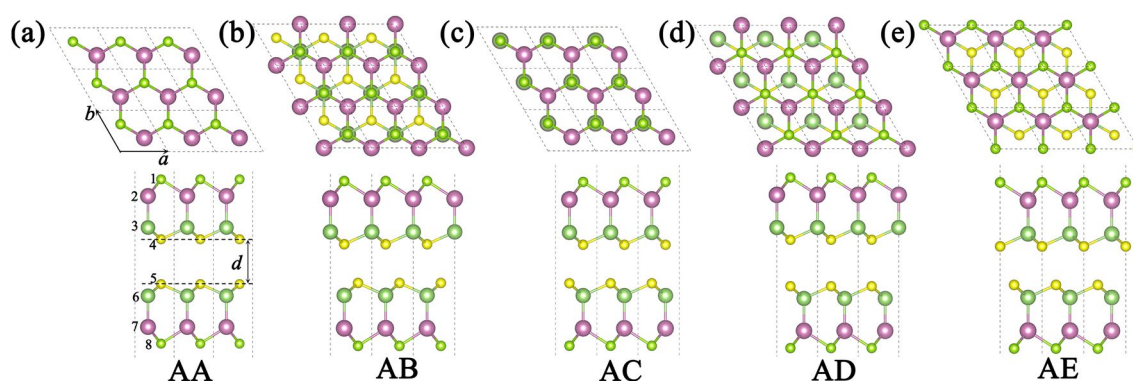


Figure 3. Top view and side view of the five models of Janus heterostructures.

| Heterostructure | a (Å) | b (Å) | d (Å) | E_g^{PBE} (eV) | CBO (eV) | PCE (%) |
|-----------------|---------|---------|---------|------------------|----------|---------|
| SSA | 3.82 | 3.82 | 3.07 | 1.103 | 0.176 | 12.8 |
| SSB | 3.83 | 3.83 | 3.03 | 1.176 | 0.604 | 6.8 |
| SSC | 3.84 | 3.84 | 3.01 | 1.304 | 0.426 | 12.9 |
| SeSeA | 3.84 | 3.84 | 3.22 | 1.238 | 0.492 | 10.3 |
| SeSeB | 3.83 | 3.83 | 3.18 | 1.039 | 0.271 | 16.2 |
| SeSeC | 3.82 | 3.82 | 3.16 | 1.035 | 0.272 | 12.7 |
| SSeB | 3.82 | 3.82 | 3.11 | 1.065 | 0.217 | 14.6 |
| SSeA | 3.83 | 3.83 | 3.14 | 1.042 | 0.241 | 13.6 |
| SSeC | 3.83 | 3.83 | 3.08 | 1.164 | 0.613 | 6.4 |
| SSeB' | 3.84 | 3.84 | 3.11 | 1.157 | 0.575 | 6.9 |

Table 3. Calculated lattice constant (a and b), interlayer distance (d), electronic band gap (E_g^{PBE}), conduction band offset (CBO) and power conversion efficiency (PCE) for different heterostructures.

in different materials, which can effectively reduce the recombination of electron-hole. Actually, the band alignment is strongly dependent on the surface termination owing to the intrinsic internal electric field of the Janus monolayer⁵⁴. The band gap of other different configurations is list in Fig. 4f. The tunable interface coupling and band alignment provide an ideal platform for promoting the effective separation of photogenerated carriers and facilitating the quantum efficiency.

To acquire the physical origin of charge transfer and charge redistribution, we calculated the plane differential charge density ($\Delta\rho$) along the z direction (see Fig. 5a,b and Fig. S5). In general, the $\Delta\rho$ can be calculated by $\Delta\rho(z) = \int \rho_{SGaInSe/SeGaInS} dx dy - \int \rho_{SGaInSe} dx dy - \int \rho_{SeGaInS} dx dy$, where $\rho_{SGaInSe/SeGaInS}$, $\rho_{SGaInSe}$ and $\rho_{SeGaInS}$ are the charge density in the heterostructure, S-Ga-In-Se and Se-Ga-In-S monolayers, respectively. It is worth noting that the electric dipole in the heterostructure contain two parts: the intrinsic electric dipole in the prime Janus monolayers and the interface dipole caused by charge redistribution⁵⁵. It is found that electron rearrangement mainly occurs in the interspace between two layers, which can induce the built-in electric dipole at the

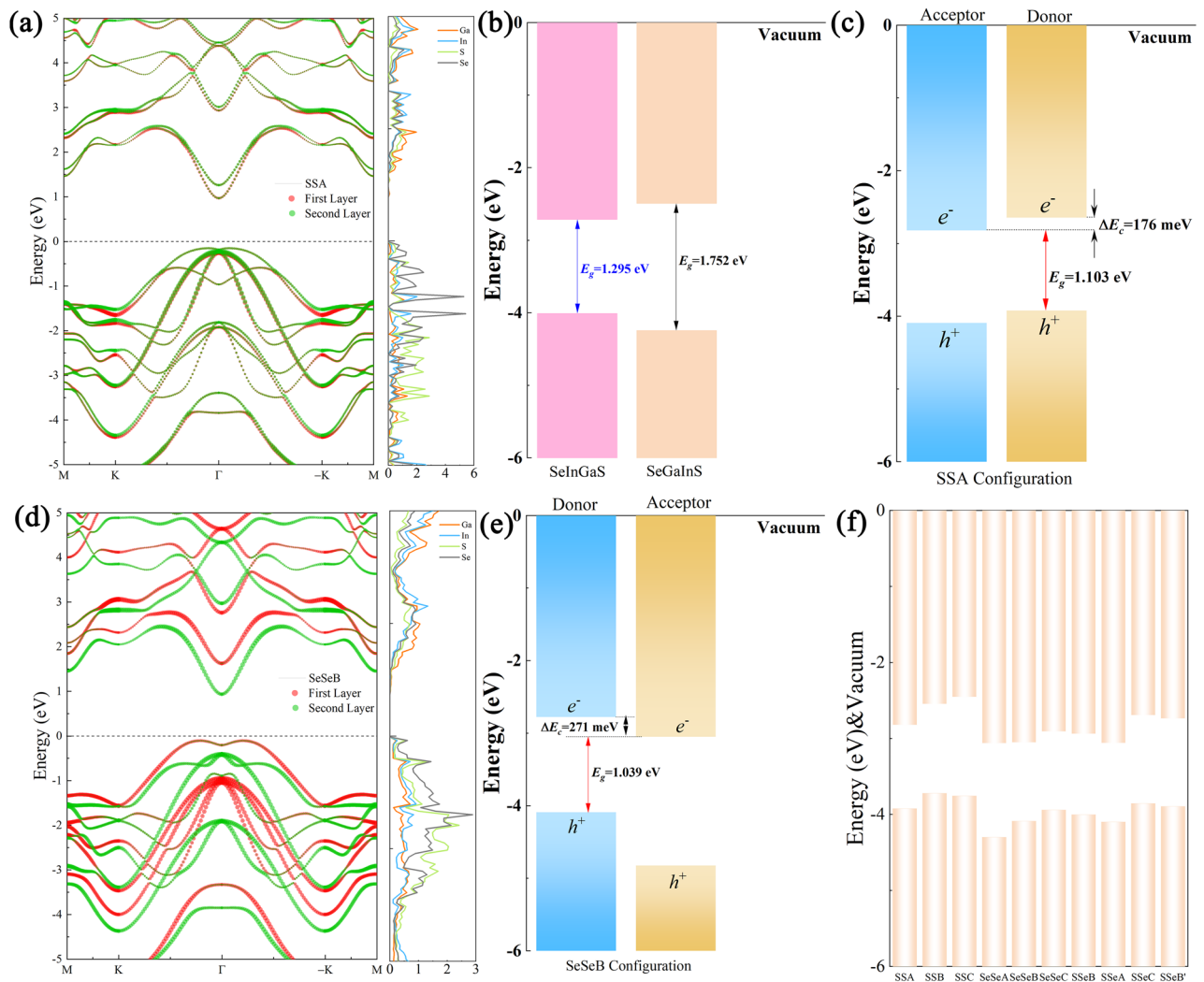


Figure 4. The band structure and DOS of the 2D Janus group-III chalcogenide for SSA (a) and SeSeB (d) configuration. (b) Band arrangement of Janus Se-In-Ga-S and S-In-Ga-Se monolayers. Band arrangement of SSA (c) and SeSeB (e) configuration. (f) Band arrangement of Janus heterostructures.

interface. Also, the Bader charge analysis showed that there is a small amount of electron transfer at the interface, resulting in an intrinsic p-n junction. The corresponding transferred charge (from first layer to second layer) for SSA, SSB, SSC, SeSeA, SeSeB, SeSeC, SSeB, SSeA, SSeC and SSeB' configuration are $-0.0011e$, $-0.0034e$, $0.0005e$, $0.0002e$, $-0.0066e$, $-0.0019e$, $0.0039e$, $0.0107e$, $0.0083e$ and $0.0143e$, which is consistent with the direction of electron transfer in the band arrangement.

In addition, we calculate the electrostatic potential difference $\Delta\Phi$ of the heterostructure, as shown in Fig. 5c,d and Fig. S6. The $\Delta\Phi$ of SSA is 0 meV, which indicates that their left and right work functions are the same because the materials on both sides have the same structure. The $\Delta\Phi$ of SeSeB configuration is 287 meV, which indicates that their left and right work functions are different because the materials on both sides have different structures. Similarly, Guo *et al.* studied the structural and optoelectronic properties of Janus aluminum monochalcogenide (C_{2h} - Al_2XY) ($X/Y=S, Se$ and Te) compounds, and found that the wider atomic size difference leads to a larger $\Delta\Phi$ ⁵⁶. Actually, the dipole in those heterostructures is associated with the stacking order, local configurations, and charge redistribution, and so on.

The optical properties of materials can be revealed by the light absorption governed by the characteristics of electronic band structures, which is the important metric for assessing viability of heterojunctions in the photoelectric devices. Generally, the light absorption coefficient can be deduced from the frequency-dependent complex dielectric function, i.e. $\alpha(\omega) = \sqrt{2}\omega/c \left[\sqrt{\varepsilon_1(\omega)^2 + \varepsilon_2(\omega)^2} - \varepsilon_1(\omega) \right]^{1/2}$, where ω is the angular frequency, c is the speed of light, ε_1 and ε_2 denotes the real and imaginary part of the dielectric function. Fig. 6a and Fig. S7 depicts the optical absorption coefficients as a function of photon energy extended from ultraviolet to visible light for in-plane light polarization. As shown, the absorption of heterostructure possess considerable visible light and near-ultraviolet absorption, which are substantially greater than those of Janus Se-In-Ga-S and S-In-Ga-Se monolayer. Meanwhile, the absorption edge of heterostructure shows an obviously red shift owing to the narrow band gap compare with the intrinsic Janus monolayers. Indeed, a narrow band gap of

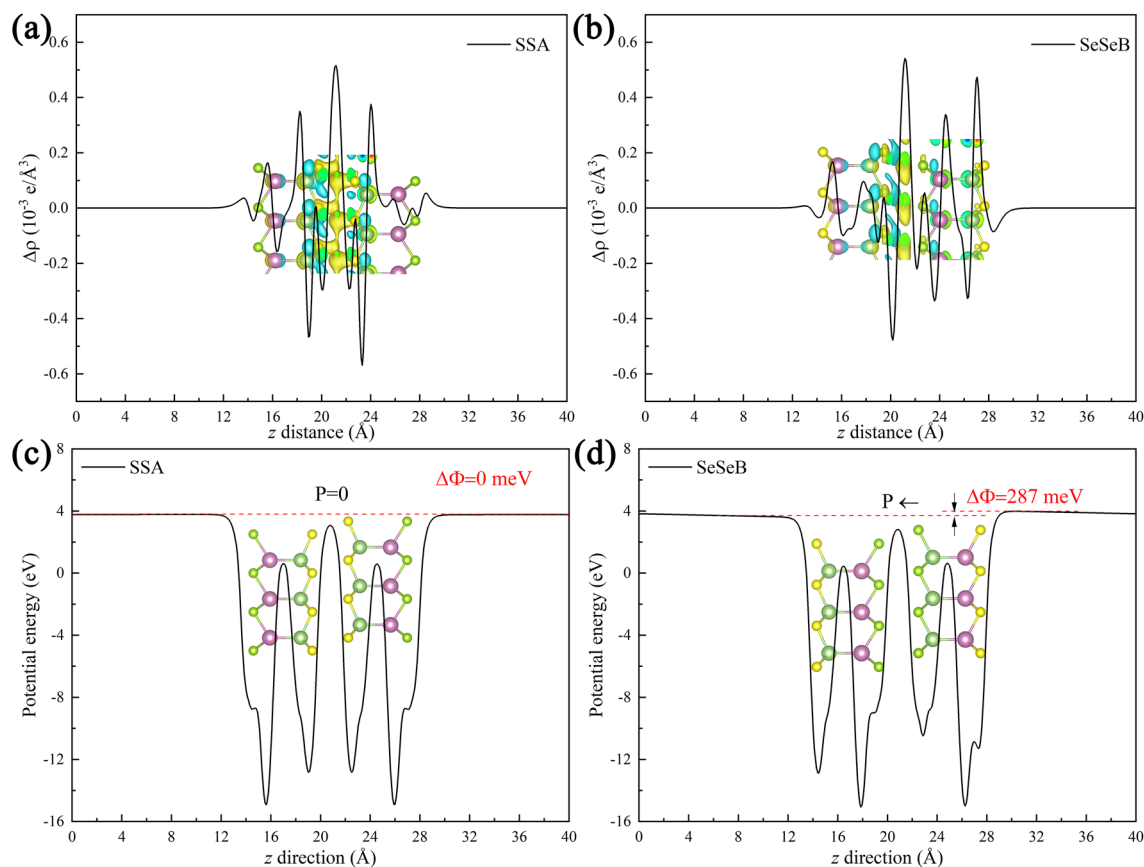


Figure 5. The charge transfer density of SSA (a) and SeSeB (b) configuration. The average potential energy of SSA (c) and SeSeB (d) configuration.

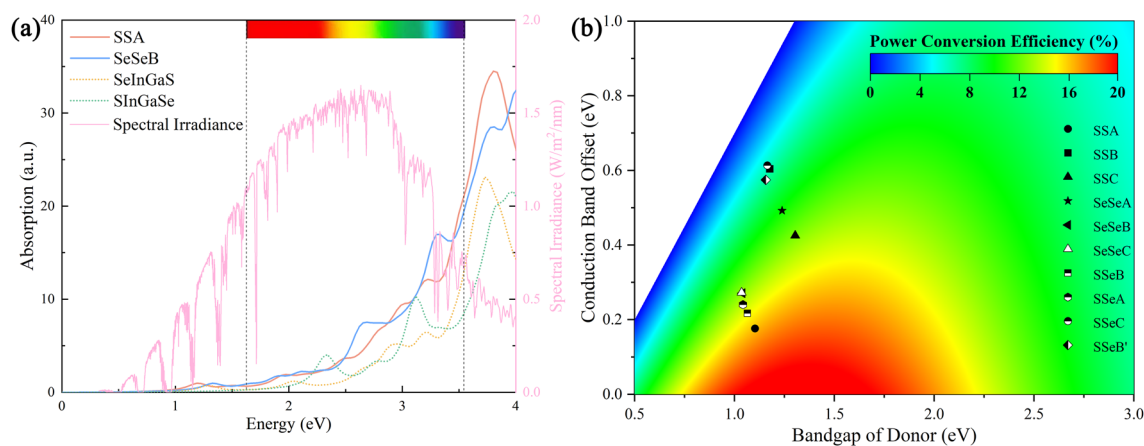


Figure 6. (a) The calculated optical absorption coefficients of SSA and SeSeB alignment, which comparison with Janus Se-In-Ga-S, S-In-Ga-Se monolayers and solar spectral irradiance. (b) The contour plot of power conversion efficiency as a function of donor domain band gap and the CBO for all type II heterostructures.

heterostructure with type II band alignment indicates a stronger absorption spectrum because it makes electron and hole pairs easier to generate.

Additionally, the range of incident solar light spectra suggests that these materials have the capacity to absorb sunlight. We carried out more research on the PCE of heterostructures in order to better understand their utilization efficiency for solar light. For heterostructures with type II band alignment, the PCE can be estimated by Scharber's method⁵⁷, i.e. $\eta = \frac{0.65(E_g^d - \Delta E_c - 0.3) \int_0^\infty P(h\nu) / h\nu d(h\nu)}{\int_0^\infty P(h\nu) d(h\nu)}$, where 0.65 is the fill factor, E_g^d is the donor band gap, ΔE_c represents the CBO, and $P(h\nu)$ is the AM1.5 solar energy flux. Fig. 6b and Table 3 shows the PCE for

all type II heterostructures. The PCE of SSeB and SSA configuration are 12.8%, and 16.2%, respectively. Actually, the PCE of heterostructure is dependent on the band gap and CBO, i.e. a suitable band gap of the donor monolayers for maximum light absorption and a lower CBO for reduced energy loss. Notably, the physical and photoelectric properties of Janus MX monolayers and based heterostructure can be effectively tuned by external factors such as electric field and strain^{58,59}. In a word, Janus MX and based heterostructures possess impressive photoelectric conversion capabilities with ultrathin thickness, indicating potential applications in photoelectric systems.

Conclusion

In summary, the fundamental characteristics of the Janus MX monolayer and ten vdW heterostructures have been systematically studied using first-principles computations. Initially, our findings suggest that the investigated monolayers are semiconducting with band gaps ranging from 1.2 eV to 1.7 eV. Bader charge analysis and electrostatic potential distribution revealed inherent electric field in Janus MX monolayers and based heterostructures. The heterostructures possess higher light absorption coefficient, intrinsic electric field and type II band alignment, which demonstrate that constructing a heterostructure is essential for high photovoltaic performance. Our findings assess the stability and excellent properties of Janus MX monolayers and based heterostructures, recommend them as promising materials for 2D photoelectric applications.

Data availability

The data that support the findings of this study are available from the corresponding author upon reasonable request.

Received: 1 February 2024; Accepted: 6 May 2024

Published online: 10 May 2024

References

- Katihar, A. K. *et al.* 2D materials in flexible electronics: Recent advances and future prospectives. *Chem. Rev.* **124**, 318–419 (2024).
- Bellani, S. *et al.* Solution-processed two-dimensional materials for next-generation photovoltaics. *Chem. Soc. Rev.* **50**, 11870–11965 (2021).
- Jiang, J., Yang, P., Liou, J. J., Liao, W. & Chai, Y. Defect engineering of two-dimensional materials towards next-generation electronics and optoelectronics. *Nano Res.* **16**, 3104–3124 (2023).
- Bafekry, A. *et al.* Ab initio prediction of semiconductivity in a novel two-dimensional Sb_2X_3 (X = S, Se, Te) monolayers with orthorhombic structure. *Sci. Rep.* **11**, 10366 (2021).
- Bafekry, A. *et al.* Semiconducting chalcogenide alloys based on the (Ge, Sn, Pb) (S, Se, Te) formula with outstanding properties: A first-principles calculation study. *ACS Omega* **6**, 9433–9441 (2021).
- Sui, F. *et al.* Sliding ferroelectricity in van der Waals layered γ -InSe semiconductor. *Nat. Commun.* **14**, 36 (2023).
- Jiang, J., Xu, L., Qiu, C. & Peng, L.-M. Ballistic two-dimensional InSe transistors. *Nature* **616**, 470–475 (2023).
- Ma, H. *et al.* High solar-to-hydrogen efficiency in the novel derivatives of group-III trichalcogenides for photocatalytic water splitting: The effect of elemental composition. *J. Mater. Chem. A* **11**, 17007–17019 (2023).
- Cheng, K. *et al.* The effect of intrinsic electric field on electronic structures: The case of polar Janus group-III monochalcogenides and their van der Waals heterostructures. *APL Mater.* **11**, 061106 (2023).
- Pang, K. *et al.* Modulation of the electronic band structure of silicene by polar two-dimensional substrates. *Phys. Chem. Chem. Phys.* **22**, 21412–21420 (2020).
- Wang, Z. *et al.* Role of Ga vacancy on a multilayer GaTe phototransistor. *ACS Nano* **8**, 4859–4865 (2014).
- Gul, S. H., Ali, B., Shafiq, M., Idrees, M. & Amin, B. Structural, optoelectronic and photocatalytic properties of MX (M=Ga, In; X=S, Se, Te) contact with novel janus GaInS₃ monolayers. *J. Solid State Chem.* **326**, 124187 (2023).
- An, J. *et al.* Perspectives of 2D materials for optoelectronic integration. *Adv. Funct. Mater.* **32**, 2110119 (2022).
- Guo, G., Xu, Y. & Guo, G. Janus-functionalization induced magnetism and improved optoelectronic properties in two-dimensional silicene and germanene: Insights from first-principles calculations. *J. Phys. Condens. Matter* **35**, 335501 (2023).
- Woods-Robinson, R. *et al.* Wide band gap chalcogenide semiconductors. *Chem. Rev.* **120**, 4007–4055 (2020).
- Zhuang, H. L. & Hennig, R. G. Single-layer group-III monochalcogenide photocatalysts for water splitting. *Chem. Mater.* **25**, 3232–3238 (2013).
- Xu, Y. H., Fan, Z. Q., Zhang, Z. H. & Zhao, T. Electronic and transport properties of GaAs/InSe van der Waals heterostructure. *Appl. Surf. Sci.* **547**, 149174 (2021).
- Ubrig, N. *et al.* Design of van der Waals interfaces for broad-spectrum optoelectronics. *Nat. Mater.* **19**, 299–304 (2020).
- Yang, X. *et al.* Tunable contacts in Graphene/InSe van der Waals heterostructures. *J. Phys. Chem. C* **124**, 23699–23706 (2020).
- Almayyali, A. O. M. & Jappor, H. R. PbBi₂Se₄ monolayer: A new 2D material with outstanding electronic, photocatalytic, and optical properties. *Solid State Sci.* **150**, 107483 (2024).
- Bafekry, A. *et al.* Investigation of vacancy defects and substitutional doping in AlSb monolayer with double layer honeycomb structure: A first-principles calculation. *J. Phys. Condens. Matter* **34**, 065701 (2022).
- Nguyen, H. T. T. *et al.* Electronic and optical properties of a Janus SnSse monolayer: Effects of strain and electric field. *Phys. Chem. Chem. Phys.* **22**, 11637–11643 (2020).
- Du, L. *et al.* Engineering symmetry breaking in 2D layered materials. *Nat. Rev. Phys.* **3**, 193–206 (2021).
- Zhao, S. *et al.* In-plane anisotropic electronics based on low-symmetry 2D materials: Progress and prospects. *Nanoscale Adv.* **2**, 109–139 (2020).
- Bafekry, A. *et al.* Puckered Penta-like PdPX (X = O, S, Te) semiconducting nanosheets: First-principles study of the mechanical, electro-optical, and photocatalytic properties. *ACS Appl. Mater. Interfaces* **14**, 21577–21584 (2022).
- Bafekry, A. *et al.* Two-dimensional Janus semiconductor BiTeCl and BiTeBr monolayers: A first-principles study on their tunable electronic properties via an electric field and mechanical strain. *Phys. Chem. Chem. Phys.* **23**, 15216–15223 (2021).
- Wang, P. *et al.* Two-dimensional In_2X_2X' (X and X' = S, Se, and Te) monolayers with an intrinsic electric field for high-performance photocatalytic and piezoelectric applications. *ACS Appl. Mater. Interfaces* **13**, 34178–34187 (2021).
- Chen, Y., Fan, Q., Liu, Y. & Yao, G. Electrically tunable magnetism and unique intralayer charge transfer in Janus monolayer MnSse for spintronics applications. *Phys. Rev. B* **105**, 195410 (2022).
- Vu, T. V. *et al.* Structural, electronic, and transport properties of Janus GaInX₂ (X = S, Se, Te) monolayers: first-principles study. *J. Phys. Condens. Matter* **34**, 045501 (2022).

30. Guo, G., Liu, J., Xu, Y., Guo, G. & Tan, S. Chemical functionalization induced photocatalytic performance for water splitting of silicene: A first-principles investigation. *Colloids Surf. A* **667**, 131379 (2023).
31. Kandemir, A. & Sahin, H. Janus single layers of In₂SSe: A first-principles study. *Phys. Rev. B* **97**, 155410 (2018).
32. Bui, H. D., Jappor, H. R. & Hieu, N. N. Tunable optical and electronic properties of Janus monolayers Ga₂SSe, Ga₂STe, and Ga₂SeTe as promising candidates for ultraviolet photodetectors applications. *Superlattices Microstruct.* **125**, 1–7 (2019).
33. Zhong, Q., Dai, Z., Liu, J., Zhao, Y. & Meng, S. Phonon thermal transport in Janus single layer M₂XY (M = Ga; X, Y = S, Se, Te): A study based on first-principles. *Phys. E* **115**, 113683 (2020).
34. Ahmad, I., Shahid, I., Ali, A., Gao, L. & Cai, J. Electronic, mechanical, optical and photocatalytic properties of two-dimensional Janus XGaInY (X, Y = S, Se and Te) monolayers. *RSC Adv.* **11**, 17230–17239 (2021).
35. Wang, Y.-Y., Li, F.-P., Wei, W., Huang, B.-B. & Dai, Y. Interlayer coupling effect in van der Waals heterostructures of transition metal dichalcogenides. *Front. Phys.* **16**, 13501 (2020).
36. Zhu, X. *et al.* Effects of interlayer coupling on the excitons and electronic structures of WS₂/hBN/MoS₂ van der Waals heterostructures. *Nano Res.* **15**, 2674–2681 (2022).
37. Hu, Z. *et al.* Interfacial charge and energy transfer in van der Waals heterojunctions. *InfoMat* **4**, 12290 (2022).
38. Singh, A., Jain, M. & Bhattacharya, S. MoS₂ and Janus (MoSSe) based 2D van der Waals heterostructures: Emerging direct Z-scheme photocatalysts. *Nanoscale Adv.* **3**, 2837–2845 (2021).
39. Xie, M. *et al.* Two-dimensional janus van der waals heterojunctions SnX₂@SnSse (X = S, Se) as promising solar-driven water-splitting photocatalysts. *ACS Appl. Energy Mater.* **7**, 31–40 (2024).
40. Ma, Z., Wang, S., Li, C. & Wang, F. Strain engineering for C₂N/Janus monochalcogenides van der Waals heterostructures: Potential applications for photocatalytic water splitting. *Appl. Surf. Sci.* **536**, 147845 (2021).
41. Min, J. *et al.* Type-II vdW heterojunction SeGa₂Te/SeIn₂Se as a high-efficiency visible-light-driven water-splitting photocatalyst. *Phys. Lett. A* **413**, 127594 (2021).
42. Guo, G., Zhang, G., Wu, H., Zhang, Y. & Xie, Z. Insights on the optoelectronic properties in two-dimensional Janus lateral In₂SeTe/Ga₂STe heterostructure. *Thin Solid Films* **718**, 138479 (2021).
43. Guo, G., Xu, C., Tan, S. & Xie, Z. Theoretical design of Janus-In₂STe/InSe lateral heterostructure: A DFT investigation. *Phys. E (Amsterdam, Neth.)* **143**, 115359 (2022).
44. Vu, T. V. *et al.* Theoretical prediction of electronic, transport, optical, and thermoelectric properties of Janus monolayers In₂XO (X=S, Se, Te). *Phys. Rev. B* **103**, 085422 (2021).
45. Xie, W., Pang, J., Yang, J., Kuang, X. & Mao, A. Highly-efficient heterojunction solar cells based on 2D Janus transition-metal nitride halide (TNH) monolayers with ultrahigh carrier mobility. *Nanoscale* **15**, 18328–18336 (2023).
46. Shu, H. & Liu, X. Interfacial electronic characteristics and tunable contact types in novel silicene/Janus Ga₂STe heterobilayers. *Surf. Interfaces* **35**, 102451 (2022).
47. Blochl, P. E. Projector augmented-wave method. *Phys. Rev. B* **50**, 17953–17979 (1994).
48. Kresse, G. & Joubert, D. From ultrasoft pseudopotentials to the projector augmented-wave method. *Phys. Rev. B* **59**, 1758–1775 (1999).
49. Perdew, J. P., Burke, K. & Ernzerhof, M. Generalized gradient approximation made simple. *Phys. Rev. Lett.* **77**, 3865–3868 (1996).
50. Guo, G., Tan, S., Guo, G. & Xie, Z. Strain-enhanced properties of Janus Si₂PA_s monolayer as a promising photocatalyst for the splitting of water: Insights from first-principles calculations. *Colloids Surf. A* **659**, 130782 (2023).
51. Heyd, J., Scuseria, G. E. & Ernzerhof, M. Hybrid functionals based on a screened Coulomb potential. *J. Chem. Phys.* **118**, 8207–8215 (2003).
52. Yu, M. & Trinkle, D. R. Accurate and efficient algorithm for Bader charge integration. *J. Chem. Phys.* **134**, 064111 (2011).
53. Mahmudov, K. T., Kopylovich, M. N., Silva, M. F. C. G. & Pombeiro, A. J. L. Chalcogen bonding in synthesis, catalysis and design of materials. *Dalton Trans.* **46**, 10121–10138 (2017).
54. Pan, H., Feng, L., Liu, P., Zheng, X. & Zhang, X. Asymmetric surfaces endow Janus bismuth oxyhalides with enhanced electronic and catalytic properties for the hydrogen evolution reaction. *J. Colloid Interface Sci.* **617**, 204–213 (2022).
55. Lin, H.-F. *et al.* Janus Ga₂SeTe/In₂SSe heterostructures: Tunable electronic, optical, and photocatalytic properties. *Phys. Chem. Chem. Phys.* **24**, 4425–4436 (2022).
56. Guo, G., Zhou, Y., Guo, G. & Xie, Z. First-principles study on the optoelectronic and photocatalytic properties of the C_{2h}-Janus Al₂XY(X/Y, S, Se and Te) monolayers. *Mater. Today Chem.* **35**, 101913 (2024).
57. Scharber, M. C. *et al.* Design rules for donors in Bulk-Heterojunction solar cells—Towards 10% energy-conversion efficiency. *Adv. Mater.* **18**, 789–794 (2006).
58. Ma, L. *et al.* Pressure and strain engineering of the structural and electronic transitions in ReS₂. *J. Phys. Condens. Matter* **35**, 365402 (2023).
59. Wu, Q., Cao, L., Ang, Y. S. & Ang, L. K. Semiconductor-to-metal transition in bilayer MoSi₂N₄ and WSi₂N₄ with strain and electric field. *Appl. Phys. Lett.* **118**, 113102 (2021).

Acknowledgements

This work was supported by the National Natural Science Foundation of China (Grant Nos.52302174 and 51802089), and the Scientific Research Fund of Hunan Provincial Education Department (Grant Nos. 22B0726, 22B0715).

Author contributions

Y. Z.: Formal analysis, Writing-Original draft preparation. Z. L., Y. W and Q. T.: Data curation, Prepared Figures. H. L.: supervision and edited the manuscript. L. M: Conceptualization, Funding acquisition and Writing-Reviewing and Editing. All authors reviewed the manuscript.

Competing interests

The authors declare no competing interests.

Additional information

Supplementary Information The online version contains supplementary material available at <https://doi.org/10.1038/s41598-024-61373-z>.

Correspondence and requests for materials should be addressed to Q.T. or L.M.

Reprints and permissions information is available at www.nature.com/reprints.

Publisher's note Springer Nature remains neutral with regard to jurisdictional claims in published maps and institutional affiliations.



Open Access This article is licensed under a Creative Commons Attribution 4.0 International License, which permits use, sharing, adaptation, distribution and reproduction in any medium or format, as long as you give appropriate credit to the original author(s) and the source, provide a link to the Creative Commons licence, and indicate if changes were made. The images or other third party material in this article are included in the article's Creative Commons licence, unless indicated otherwise in a credit line to the material. If material is not included in the article's Creative Commons licence and your intended use is not permitted by statutory regulation or exceeds the permitted use, you will need to obtain permission directly from the copyright holder. To view a copy of this licence, visit <http://creativecommons.org/licenses/by/4.0/>.

© The Author(s) 2024